# Supplementary Material

## Hydro-photo-synergy unlocks deep and reversible chemistry of solid-state lithium-oxygen batteries

*Sijia Chi*[1,2,3], *Zhenshen Li*[1,2,3], *Xunjie Yin*[1,2,3], *Shuoyi Chen*[1,2,3], *Xuerui Yi*[1,2,3], *Yiqiao Wang*[1,2,3], *Yong Guo*[1,2,3], *Fangbing Li*[1,2,3], *Shichao Wu*[1,2,3]* *and Quan-Hong Yang*[1,2,3,4]

[1] Nanoyang Group, Tianjin Key Laboratory of Advanced Carbon and Electrochemical Energy Storage, School of Chemical Engineering and Technology, National Industry-Education Integration Platform of Energy Storage, and Collaborative Innovation Centre of Chemical Science and Engineering, Tianjin University, Tianjin 300072, China

[2] State Key Laboratory of Chemical Engineering and Low-Carbon Technology, Tianjin University, Tianjin 300072, China

[3] Haihe Laboratory of Sustainable Chemical Transformations, Tianjin, 300192, China

[4] Joint School of National University of Singapore and Tianjin University, International Campus of Tianjin University, Binhai New City, Fuzhou 350207, China

19 **Figures and Tables**

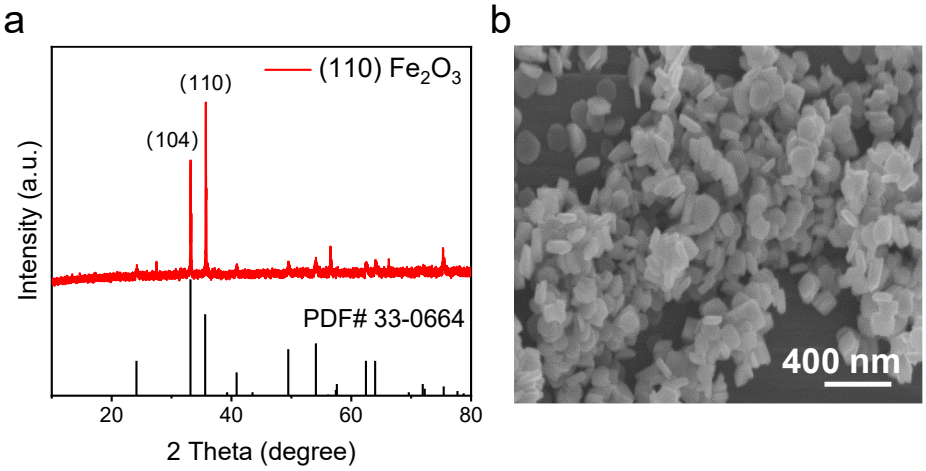


20

21 Fig. S1 (a) XRD patterns of (110) $Fe_2O_3$. (b) SEM images of (110) $Fe_2O_3$.

22

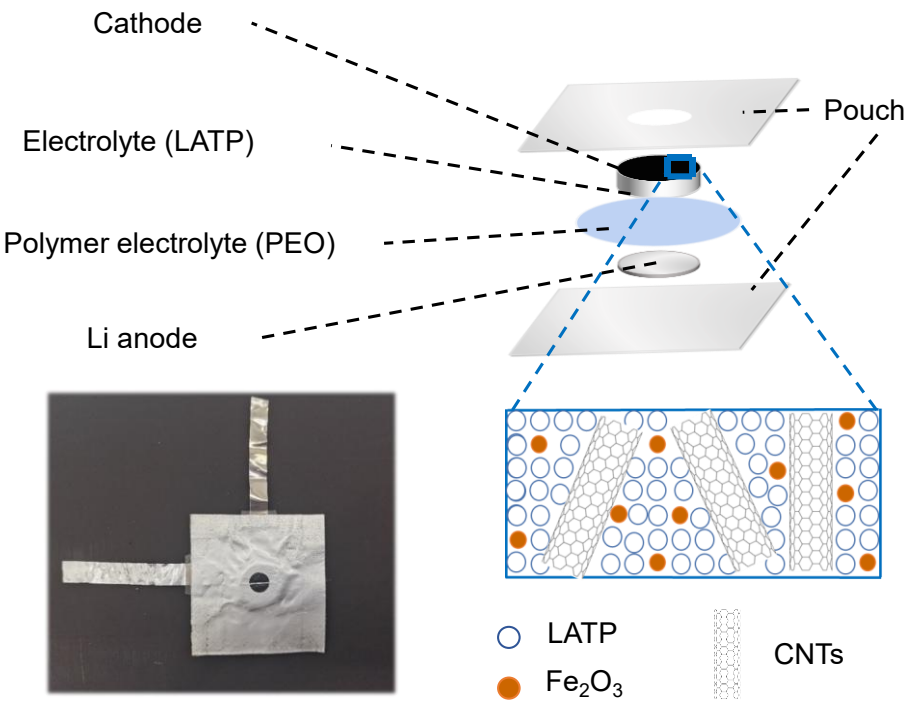


Fig. S2 Schematic illustration of proposed solid-state Li-$O_2$ battery.

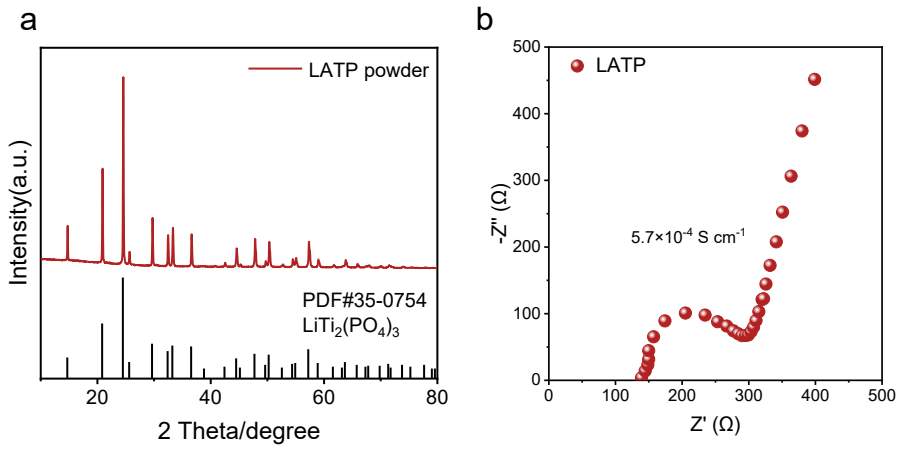


Fig. S3 (a) the XRD pattern of the solid-state LATP electrolytes and standard PDF card for $LiTi_2(PO_4)_3$ (JCPDS#35-0754). (b) Nyquist plot of LATP with symmetric Au blocking electrodes over the frequency range 0.1 Hz to 1 MHz.

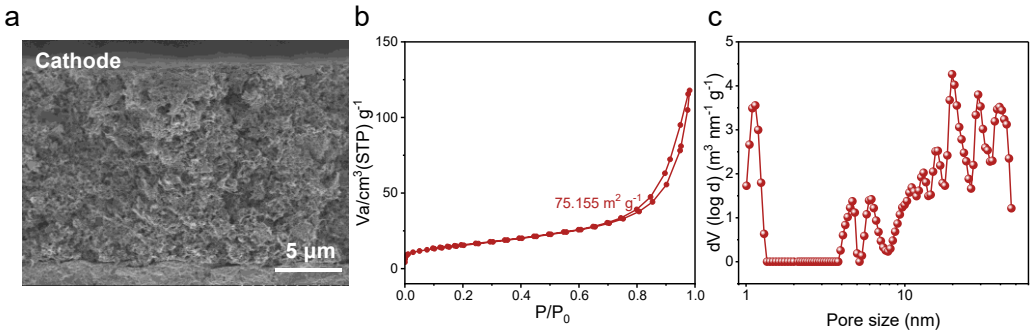


Fig. S4 SEM image and BET curves of the pore structure of the cathode.

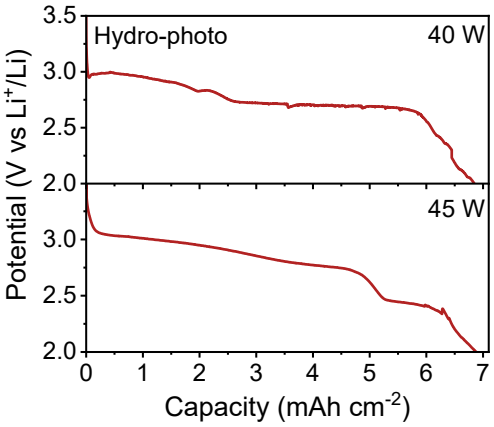


Fig. S5 Discharge voltage profiles at intensities of 40W and at 45W under hydro-photo.

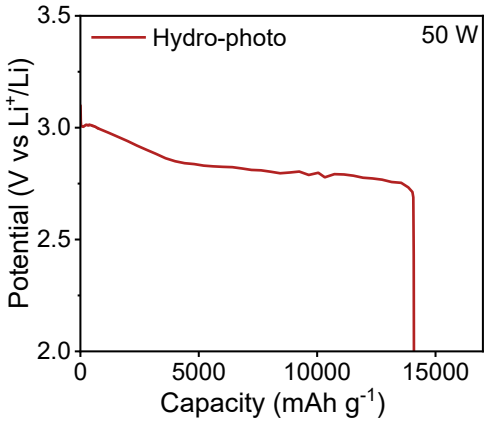


Fig. S6 Discharge curve at an illumination intensity of 50 W under hydro-photo.

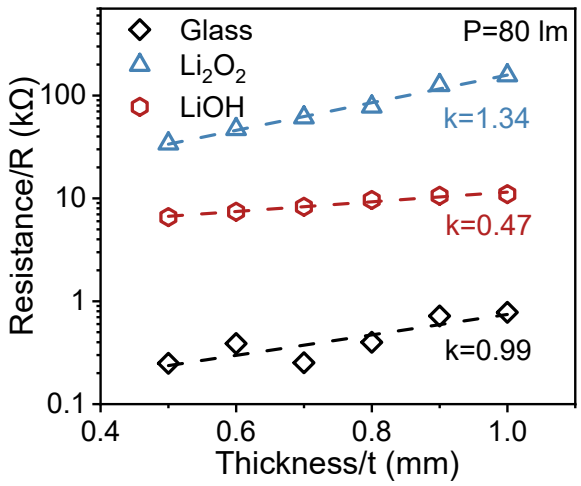


Fig. S7 Transparency test results of $Li_2O_2$, LiOH and glass at same distance and illumination intensity at 80 lm.

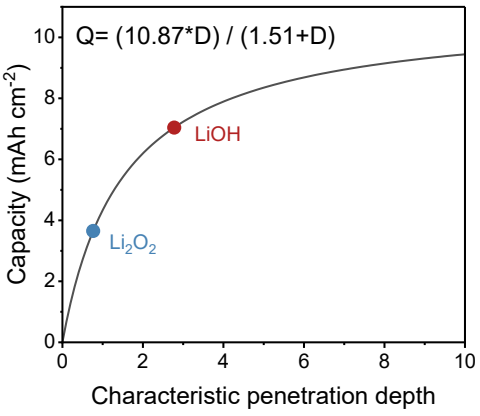


Fig. S8 The fitting curve of characteristic penetration depth and capacity.

The specific calculation steps are: R of the photoresistor relates to the incident light intensity through the power law equation where $\gamma$ is a characteristic constant of the semiconductor material (typically 0.6–0.9).

$$R \propto I^{-\gamma} \quad (1)$$

Combining Eqs. $I(z) = I_0 e^{-k_{opt} d}$ and (1)

$$R \propto \left(I_0 \cdot e^{-k_{opt} d}\right)^{-\gamma} \quad (2)$$

Taking the logarithm of both sides and rearranging yields the linear relationship

$$\ln R = \left(\gamma \cdot k_{opt}\right) \cdot d + C \quad (3)$$

The relationship implies that the logarithm of resistance scales linearly with product thickness. As delineated in Fig. 3h, the post-fitting slope (k)corresponds to the $\gamma \cdot k_{opt}$. Since $\gamma$ is a constant that affects both samples identically, we herein define k as the effective attenuation coefficient. It elucidates the thickness-dependent transparency evolution mechanism, i.e., the smaller k is, the less the transparency of the material is affected by the thickness. Crucially, the transparency of $Li_2O_2$ degrades rapidly with increasing thickness (k=1.31), whereas LiOH maintains its high transparency much more effectively (k=0.36), even better than glass (k=0.71) (Fig. 3h, i). The characteristic penetration depth

($D$) is defined as the propagation distance at which the incident light intensity decays to $1/e$ of its initial value. In accordance with the Beer-Lambert law, this physical quantity is mathematically equivalent to the reciprocal of the $k$, expressed as $D = 1/k$. This parameter directly dictates the effective spatial range of the photocatalytic reaction within the electrode. Based on the calculated attenuation coefficients, the penetration depths were determined to be $D_{Li_2O_2} = 0.763$ and $D_{LiOH} = 2.778$. Subsequently, a Langmuir saturation model was employed to describe the quantitative relationship between $Q$ and $D$.

$$Q = (Q_{max} \cdot D)/(K + D) \quad (4)$$

Here $Q_{max}$ represents the intrinsic geometric capacity limit of the cathode architecture. It signifies the maximum amount of discharge product that can be physically accommodated within the electrode's porous structure, assuming that optical attenuation is completely negligible and K is the half-saturation constant, defined as the optical penetration depth required to achieve 50% of the theoretical maximum capacity. It serves as a critical threshold indicator: reaction kinetics are optically limited when the penetration depth is below K, and spatially limited (pore-filling dominated) when significantly above K.By substituting the experimental data points ($D_{Li_2O_2} = 0.763, Q_{Li_2O_2} = 3.65; D_{LiOH} = 2.778, Q_{LiOH} = 7.04$) into the proposed model, the critical parameters were calculated to be $Q_{max} = 10.87\ mAh$ and $K = 1.51$. Consequently, the quantitative relationship between $Q$ and $D$ is expressed as $Q = 10.87D/(1.51 + D)$, as illustrated in Fig. S8.

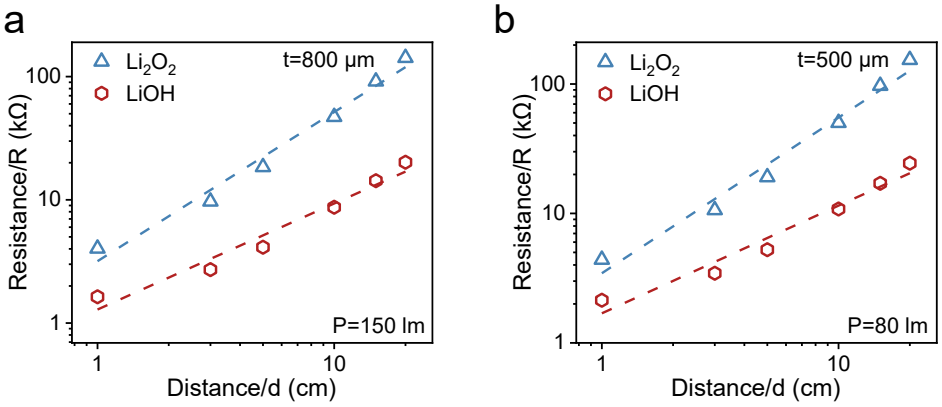


86

87 Fig. S9 Transparency test results of $Li_2O_2$ and LiOH at different distance and illumination

88 intensity.

89

90

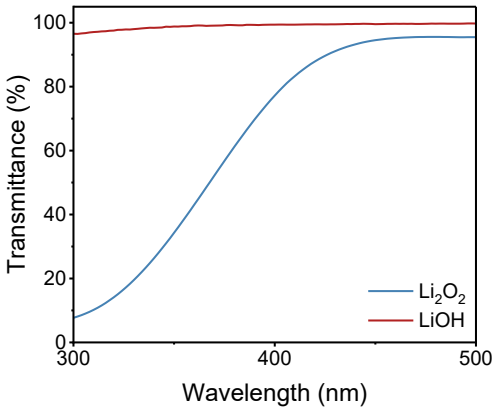


91

92 Fig. R10 The UV-visible spectra of $Li_2O_2$ and LiOH.

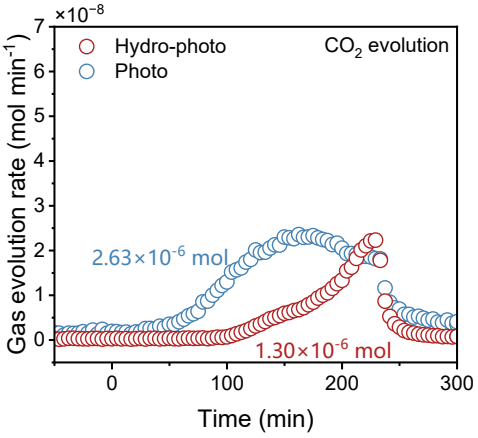


93

94 Fig. S11 The reduction and evolution of $CO_2$ under photo and hydro-photo.

95

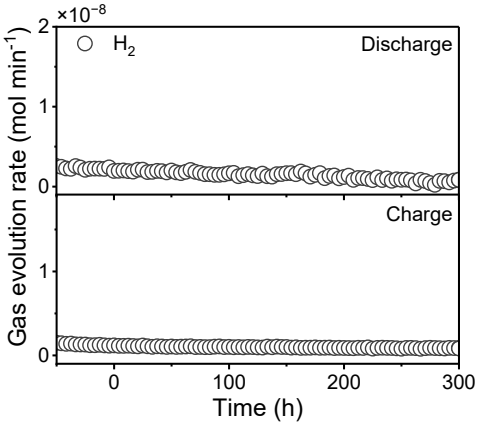


96

97 Fig. R12 The reduction and evolution of $H_2$ under hydro-photo.

98

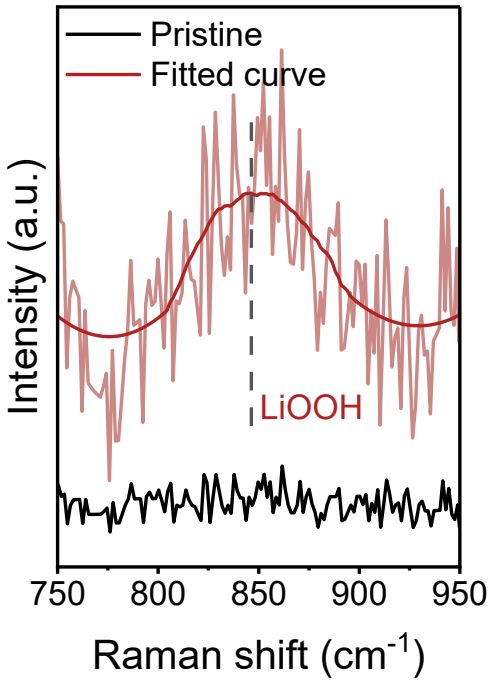


99

100 Fig. R13 FTIR confirm the intermediate is LiOOH under hydro-photo.

101

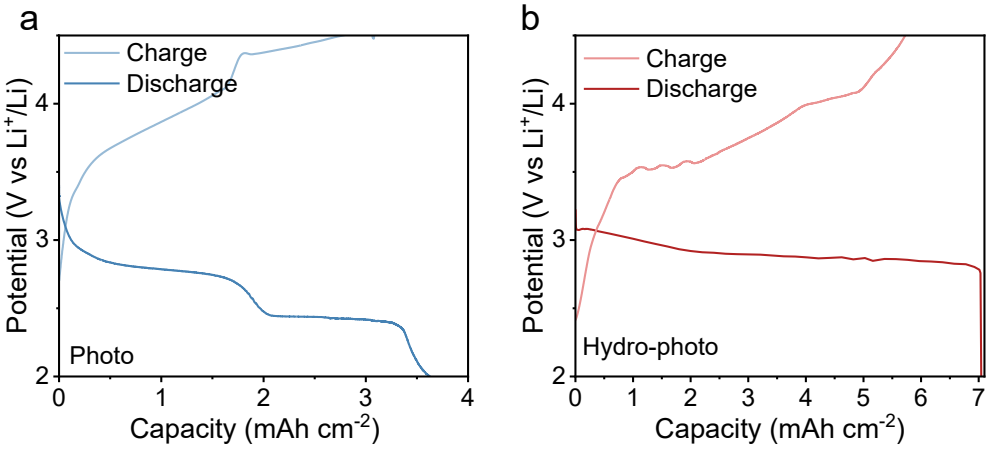


102

103 Fig. S14 Discharge/charge curves under two conditions.

104

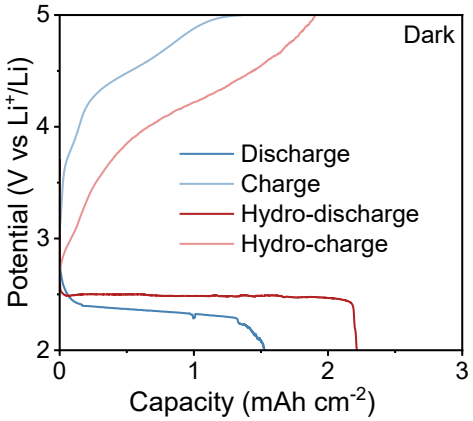


Fig. S15 Discharge/charge curves under dark.

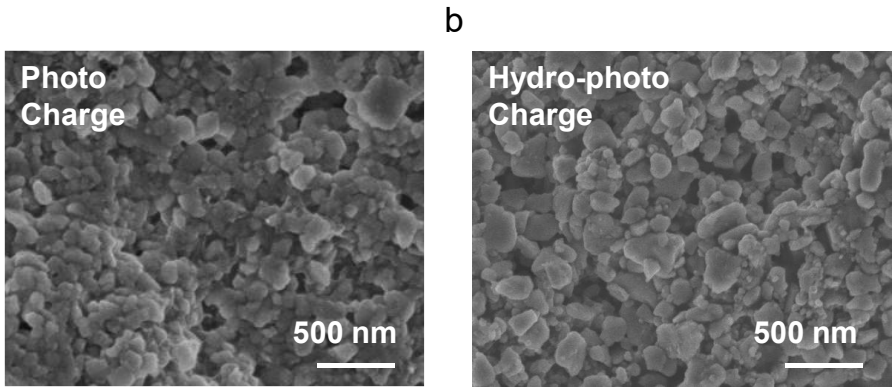


Fig. S16 SEM images of the cathode after charge under (a) photo and (b) hydro-photo.

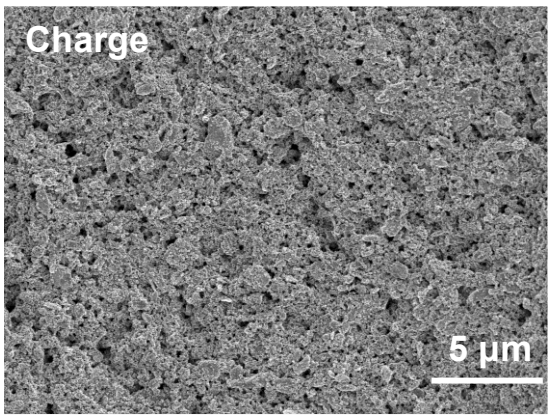


Fig. S17 SEM image of the cathode after charge under hydro-photo.

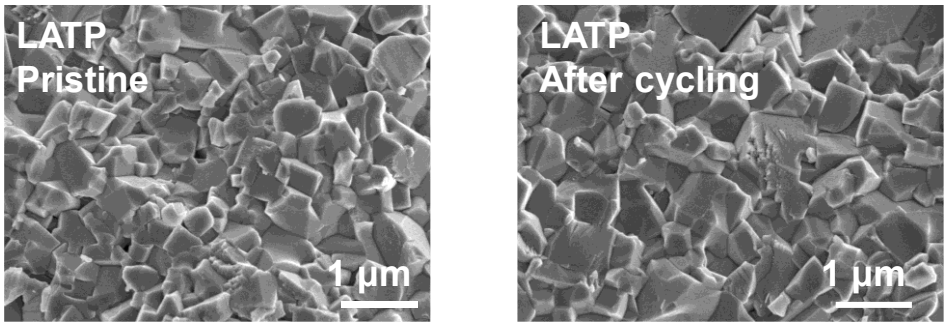


Fig. S18 SEM images of LATP before and after cycling.

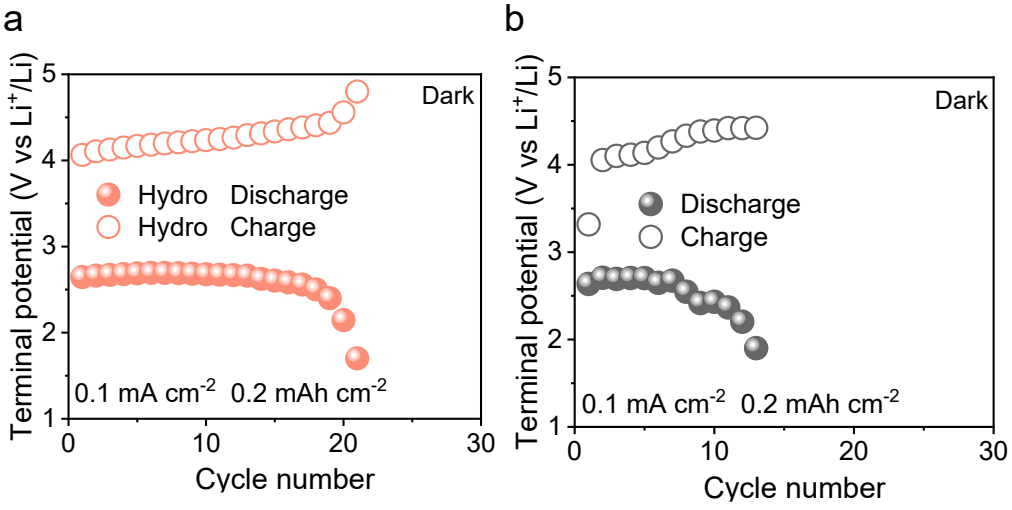


Fig. S19 Cycling performance under different conditions.

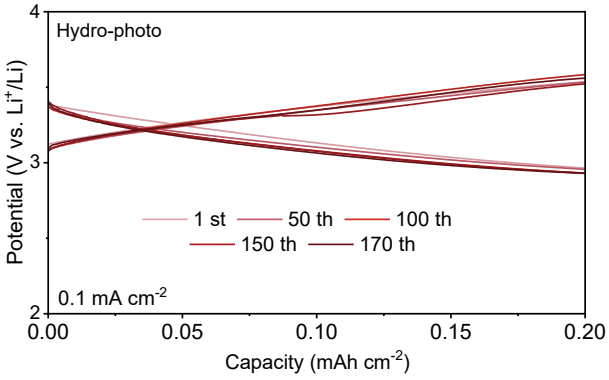


120

121 Fig. S20 Cycling performance under hydro-photo at a cut-off capacity of 0.2 mAh $cm^{-2}$.

122

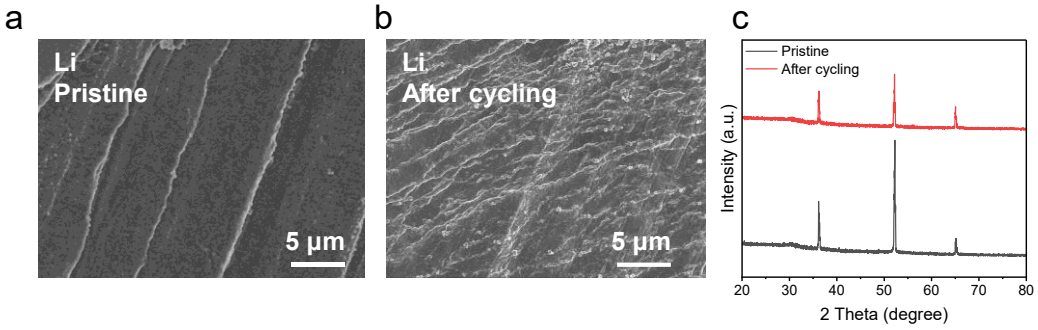


123

124 Fig. S21 SEM images and XRD analyses of the lithium anode before and after
125 cycling.

**Table S1** Resistance-value of photoresistor for photo transmission through different materials at an intensity of 150 lm.

| 150 lm | | | |
|---|---|---|---|
| | Glass | $Li_2O_2$ | LiOH |
| Thickness (μm) | Resistance (kΩ) | | |
| 500 | 0.203 | 17.857 | 3.717 |
| 600 | 0.261 | 19.317 | 4.457 |
| 700 | 0.332 | 30.737 | 4.937 |
| 800 | 0.363 | 45.137 | 5.737 |
| 900 | 0.43 | 81.587 | 6.267 |
| 1000 | 0.467 | 90.087 | 6.577 |

**Table S2** Resistance-value of photoresistor for photo transmission through different materials at an intensity of 80 lm.

| 80 lm | | | |
|---|---|---|---|
| | Glass | $Li_2O_2$ | LiOH |
| Thickness (μm) | Resistance (kΩ) | | |
| 500 | 0.186 | 26.321 | 5.601 |
| 600 | 0.249 | 34.041 | 6.581 |
| 700 | 0.388 | 47.031 | 7.421 |
| 800 | 0.252 | 61.091 | 8.281 |
| 900 | 0.399 | 77.891 | 9.641 |
| 1000 | 0.718 | 125.891 | 10.611 |

**Table S3** Previous reports on the performance of photo-assisted Li-$O_2$ battery systems, most of which illustrating limited capacity. See details according to the references.

| Photocatalyst | Electrolyte | Current density (mA $cm^{-2}$) | Cut-off capacity (mAh $cm^{-2}$) | Cycle | Total capacity (mAh $g^{-1}$) | Refs. |
|---|---|---|---|---|---|---|
| g-$C_3N_4$ | LiTFSI/TEGDME | 0.01 | 0.01 | 70 | 975 | [1] |
| $C_3N_4$ | $LiClO_4$/TEGDME | 0.1 | 0.1 | 10 | 1000 | [2] |
| $TiO_2$–$Fe_2O_3$ | $LiCF_3SO_3$/TEGDME | 0.05 | 0.1 | 120 | 1160 | [3] |
| Fe-UiO-66 | LiTFSI/TEGDME | 0.01 | 0.02 | 500 | 4166.666667 | [4] |
| $CeVO_4$ | LiTFSI/TEGDME | 0.15 | 0.15 | 50 | 13644.44444 | [5] |
| p-$MoS_2$ | LLZTO-PEO | 0.1 | 0.05 | 170 | - | [6] |
| $Fe_2O_3$/$C_3N_4$ | LiTFSI/TEGDME | 0.4 | 0.4 | 50 | - | [7] |
| $MoS_2$/$ZnIn_2S_4$ | LiTFSI/TEGDME | 0.05 | 0.05 | 130 | 5857.142857 | [8] |
| Siloxene NSs | LiTFSI/DMSO | 0.075 | 0.15 | 100 | 1170 | [9] |
| $WO_3$ | LiTFSI/TEGDME | 0.06 | 0.06 | 100 | 10500 | [10] |
| **Our report** | **LATP** | **0.1** | **0.2** | **170** | **14000** | |

References


1 Y. Liu, N. Li, K. Liao, Q. Li, M. Ishida and H. Zhou, *J. Mater. Chem. A*, 2016, **4**, 12411–12415.

2 Z. Zhu, X. Shi, G. Fan, F. Li and J. Chen, *Angew. Chem. Int. Ed.*, 2019, **58**, 19021–19026.

3 M. Li, X. Wang, F. Li, L. Zheng, J. Xu and J. Yu, *Adv. Mater.*, 2020, **32**, 1907098.

4 Y. Yang, X. Hu, G. Wang, J. Han, Q. Zhang, W. Liu, Z. Xie and Z. Zhou, *Adv. Funct. Mater.*, 2024, **34**, 2315354.

5 D. Li, X. Lang, Y. Guo, Y. Wang, Y. Wang, H. Shi, S. Wu, W. Wang and Q.-H. Yang, *Nano Energy*, 2021, **85**, 105966.

6 L. Ren, M. Zheng, F. Kong, Z. Yu, N. Sun, M. Li, Q. Liu, Y. Song, J. Dong, J. Qiao, N. Xu, J. Wang, S. Lou, Z. Jiang and J. Wang, *Angew. Chem. Int. Ed.*, 2024, **136**, e202319529.

7 Z. Zhu, Q. Lv, Y. Ni, S. Gao, J. Geng, J. Liang and F. Li, *Angew. Chem. Int. Ed.*, 2022, **61**, e202116699.

8 H. Gong, T. Wang, K. Chang, P. Li, L. Liu, X. Yu, B. Gao, H. Xue, R. Ma, J. He and J. Ye, *Carbon Energy*, 2022, **4**, 1169–1181.

9 C. Jia, F. Zhang, L. She, Q. Li, X. He, J. Sun, Z. Lei and Z.-H. Liu, *Angew. Chem. Int. Ed.*, 2021, **60**, 11257–11261.

10 M. Wang, J. Chen, Z. Tian, W. Dai, B. Cui, X. Cui, D. Wang, Y. Xiao, X. Lian, C. Jiang, H. Yang, Y. Wang, Z. Sun, Y. Ding, Y.-Y. Sun, J. Zhang and W. Chen, *Energy Environ. Sci.*, 2023, **16**, 523–534.